Impact of a transmitting-RIS on the geometrical structure of indoor mmWave channels

Alfred Mudonhi, Marina Lotti, Antonio Clemente, Raffaele d'Errico, Claude Oestges

Impact of a Transmitting-RIS on the Geometrical Structure of Indoor mmWave Channels

Alfred Mudonhi*†‡, Marina Lotti*†, Antonio Clemente*†, Raffaele D'Errico*†, Claude Oestges‡

*CEA-Leti, Grenoble, France, alfred.mudonhi@cea.fr, marina.lotti@cea.fr, antonio.clemente@cea.fr, raffaele.derrico@cea.fr

†Université Grenoble-Alpes, Grenoble, France

‡ICTEAM-Universite catholique de Louvain, Belgium, claude.oestges@uclouvain.be

Abstract—In this paper we investigate the impact of the use of Transmitting Reconfigurable Intelligent Surfaces (T-RISs) on the indoor millimeter wave (mmWave) radio channel characteristics. To this purpose, two measurement campaigns were conducted by employing a T-RIS array and a virtual cubic array (VCA). The multipath component extraction was performed to embed the T-RIS based antenna pattern and evaluate the effect on large-scale parameters such as the path loss, delay and angular spreads.

Index Terms—Indoor Propagation, Millimeter waves, Massive MIMO, Reconfigurable Intelligent Surfaces, Transmitarray.

I. INTRODUCTION

In the development of 5G and beyond networks, millimeter waves (mmWave) technologies are expected to play a significant role in attaining enhanced performances (ultra-high throughput and ultra-low latency). These technologies are often considered in combination with massive multiple-input multiple-output (mMIMO) transmission and beamforming antennas to counteract the poor link budgets [1]. mMIMO technology involves the deployment of numerous antennas, generally at the base station, in order to increase channel capacity, link reliability, and eventually provide enhanced security [2], [3]. Literature has been focusing on sub−6 GHz mMIMO channels, showing the benefits of these approaches [4], [5].

Reconfigurable Intelligent Surfaces (RIS) are nowadays considered as a new paradigm for wireless communication [6]. The interaction with electric and/or magnetic fields, is typically provided by resonant effects controlled by the geometry of the unit cells and their distribution, enabling antenna performance enhancement (beamshaping), flat lens, artificial magnetic conductors, cloaking, absorbers and scattering reduction. Indeed, one of the use of these surfaces is to realize reflect- or transmitarrays as solutions for applications requiring high gain and efficiency, and wide field of view (>60°) scanning capabilities. These technologies have recently emerged as a promising alternative to the traditional phased arrays. In the scope of 6G (sixth generation), the work in [7] provides an overview on how the emerging technology of RISs will enable the concept of the wireless environment as a service.

In the past, fixed beam transmitarrays have already been used for channel characterization in the V-band for backscattering measurements [8], and preliminary results of T-RIS based antenna in the Ka band have been presented in [9] and have shown the impact of surface based beamforming.

In this paper we extend the results of [9] to evaluate how the structure of the channel is geometrically modified when a Transmitting-Reconfigurable Intelligent Surface (T-RIS) is employed. To this purpose, the one-plane omnidirectional channel is characterized in the same environment by using a Virtual Cubic Array (VCA) in Sec. II. The multipath components (MPCs) are extracted from VCA measurements by means of Ultra-wideband Space-Alternating Generalized Expectation-Maximization (UWB-SAGE) algorithm in Sec. III. The T-RIS based antenna pattern for a given phase distribution is embedded on the omnidirectional Power Angular Delay Profile (PADP) extracted from VCA and then compared with measurements. Finally the impact of Dense Multipath Components (DMCs) are briefly discussed in Sec. IV. Sec. V concludes the paper.

II. CHANNEL MEASUREMENT CAMPAIGN AND SETUP

In this section we describe two indoor channel measurement campaigns performed by employing a T-RIS (Fig. 1 (a)) or a VCA antenna (Fig. 1 (b)).

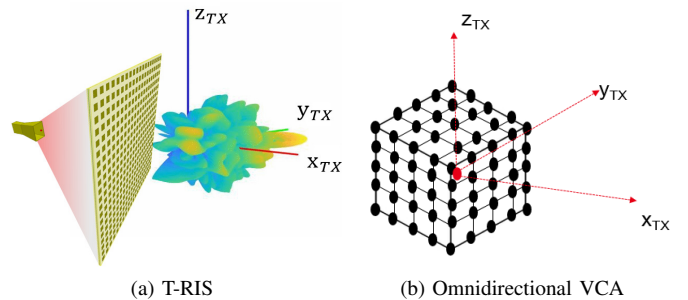(a) T-RIS   (b) Omnidirectional VCA

Fig. 1. T-RIS based antenna (a) and VCA (b) schemas.

The channel measurements were conducted in a laboratory room. The dimensions of the room were $12\ m \times 6\ m$. The laboratory room is furnished with tables, chairs, desktops, sofas, and a television as clearly depicted in the Fig. 2(a) and Fig. 2(b). The left wall of the room comprises mostly of glass windows and the right side wall also has a part with a glass window. On the roof, there is also a metallic positioner. The measurement setup is based on a Vector Network Analyzer (VNA) operating in the frequency range 26-30 GHz. The receive side (RX) and the transmit side (TX)
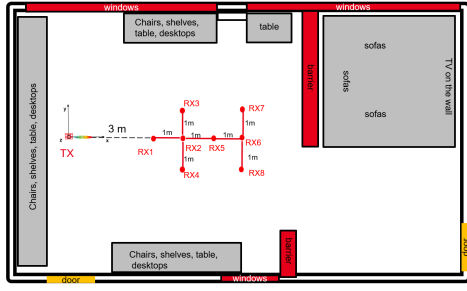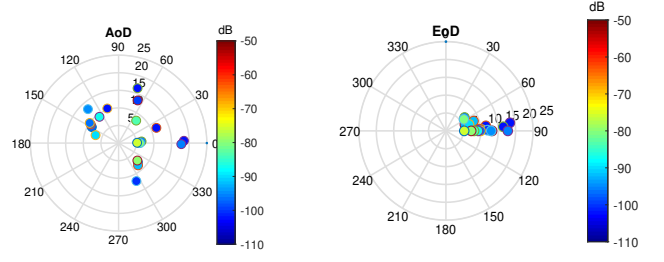
(a) Floor plans

(b) Environment

Fig. 2. Indoor channel measurement campaign : measurement floor plan (a) and environment (b).

(a) (b)

Fig. 3. Power Angular Delay Profile (PADP) extracted from VCA measurements in the azimuth plane (a) and elevation plane (b) for receiver position RX5.

Let us consider the angular dependent channel impulse response extracted from VCA measurements as:

$$h(\tau, \Omega_{AoD}, \Omega_{AoA}) = \sum_{l=1}^{L} \alpha_l \cdot \delta(\tau - \tau_l) \cdot \delta(\Omega_{AoD} - \Omega_{AoD,l})$$
$$\cdot \delta(\Omega_{AoA} - \Omega_{AoA,l}) \quad (1)$$

where the l-th MPC is characterized by its amplitude (α_l), delay (τ_l), angle of departure $\Omega_{AoD,l}$ and angle of arrival $\Omega_{AoA,l}$. Starting from this estimation, the objective is to embed T-RIS effect on the channel and compare it with the real measured one with the T-RIS.

The T-RIS vector transfer function can be written as:

$$\mathbf{H}(f, \theta, \phi, \theta_s, \phi_s) = \sum_m \frac{\lambda}{4\pi r_m} e^{-\frac{j2\pi}{\lambda} r_m} \mathbf{H}_{FS}\left(\theta_{FS}^m, \phi_{FS}^m\right) \cdot$$
$$\mathbf{H}_{RX,m}\left(\theta_{uc}^m, \phi_{uc}^m\right) \cdot \mathrm{S}_{21}^m(f) \cdot \mathbf{H}_{TX,m}\left(\theta_{uc}^m, \phi_{uc}^m\right) \quad (2)$$

where $\mathbf{H}_{FS}\left(\theta_{FS}^m, \phi_{FS}^m\right)$ is the radiation pattern of the source illuminating the surface, $\mathbf{H}_{RX,m}\left(\theta_{uc}^m, \phi_{uc}^m\right)$, $\mathbf{H}_{TX,m}\left(\theta_{uc}^m, \phi_{uc}^m\right)$ respectively represent the radiation patterns of the m-th unit-cell in the receiving side and of the m-th unit-cell in the transmitting side. r_m represents the distance between the source and the m-th unit-cell. Each unit cell will present a transmission coefficient $\mathrm{S}_{21}^m(f)$, whose phase is controlled by a 1-bit PIN diode architecture, implementing either a $0°$ or $180°$ variation. f is the frequency index, θ, ϕ are the pattern elevation and azimuthal angles respectively. Finally θ_s, ϕ_s are the elevation and azimuthal steering angles, obtained thanks to the phase distribution over the unit-cells.

Hence for a given phase distribution on the T-RIS, i.e. for an aimed steering angle (θ_s, ϕ_s), we can embed its effect on the channel by replacing in Eq. (1) the l-th MPC amplitude with:

$$\alpha_l^{emb} = \alpha_l \cdot H(f, \theta = \theta_{AoD,l}, \phi = \phi_{AoD,l}, \theta_s, \phi_s) \quad (3)$$

where $H(f, \theta = \theta_{AoD,l}, \phi = \phi_{AoD,l}, \theta_s, \phi_s)$ is the transfer function of the T-RIS from Eq. (2) in the given angle of departure $\Omega_{AoD,l} = (\theta_{AoD,l}, \phi_{AoD,l})$, neglecting here the

were both at a height of 1.52 m above the ground. While on the RX side a wideband monopole (around 0 dBi gain) antenna was employed in both setups, two different strategies were implemented on the TX.

The T-RIS based measurement setup (Fig. 1 (a)) is based on 20×20 surface elements implementing a circularly polarized transmitarray [9], [10], presenting 18.7 dBic in the main steering direction, $\phi_s = 0°$, while at maximum steering angle investigated, i.e. $\phi_s = \pm 60°$ the gain drops to 11.94 dBic, because of the array factor effect. In this measurement campaign for each RX position, different phase distribution on the 400 unit cells are implemented to scan the environment and vary the main steering direction ϕ_s, from -60° to 60° by step of 5°. In the VCA setup, a wideband monopole antenna placed on a X-Y-Z scanner performs a $5 \times 5 \times 5$ spatial grid of a half-wavelength grid step, i.e. 5 mm (Fig. 1 (b)).

III. MULTIPATH ESTIMATION AND RIS PATTERN EMBEDDING

Starting from the VCA channel measurements, the UWB-SAGE algorithm was used [11] for the MPCs detection and channel parameters estimations. MPCs of significant powers were considered in this work (10 dB above the noise floor). The maximum number of resolvable MPCs to be estimated was set to 100. The stopping criteria was when more than 95 percent of the measured channel power had been estimated, or otherwise, when the maximum number of the resolvable MPCs had been reached. Fig. 3 shows the azimuth angle of departure (AoD) and elevation angle of departure (EoD) polar plots for the receiver position RX5: each circle on the figures represents a detected MPC, whose color is the power and the radial distance is the traveled distance in meters.

polarization for simplicity of notation. In practice, given that we used on RX side a vertically polarized antenna, we consider in the following analysis the embedding with only the main polarization (given the small effect from the cross-polarised contribution).

IV. RESULTS

A. Measured Channel vs Synthesized Channels

In this section, we will discuss the main results obtained. For the receiver positions RX1, RX2, RX5 and RX6, the steering angle $\phi_{s,max}$, corresponding to the main lobe direction where the maximum power is received, is $\phi_{s,max} = 0°$, while for the receiver positions RX3, RX4, RX7 and RX8, the main beams are in the steering directions $\phi_{s,max} = 15°, -15°, 10°$, and $-10°$ respectively. In [9], the T-RIS was found to decrease both the path loss and delay spread (DS) for all receiver positions in the main lobe direction. As an example we consider here RX5 position. Fig. 4 shows the UWB-SAGE estimated MPCs, i.e. the Power Angular Delay Profile (PADP) with omnidirectional antennas. We then consider T-RIS embedding in the full 3D plane or just 2D plane, hence forcing $\theta_{AoD,l} = 90°$. Fig. 5(a) shows the 2D pattern embedding at the position RX5 for $\phi_{s,max} = 0°$. We can see that the embedding process results in some significant paths whose AoDs do not lie within the T-RIS range $[-90° : 1° : 90°]$ being eliminated. We can also see that the power of the MPCs whose AoDs are within the half power beamwidth (HPBW) are amplified while those outside HPBW are decreased when the embedding is performed using the radiation pattern for $\phi_{s,max} = 0°$. A similar behaviour is observed for the other receiver positions when embedded with the radiation patterns corresponding to ϕ_s. Fig. 5(b) shows the 3D radiation pattern embedding ($\phi_{s,max} = 0°$), which takes into account both the azimuth and elevation planes for the position RX5. We can notice that some significant paths whose AoDs do not lie within the T-RIS range $[-90° : 1° : 90°]$ were eliminated. On top of this, we can clearly see in Fig. 5(b) that 3D embedding impacts the MPCs in both the azimuth and elevation planes. Considering the T-RIS patterns for $\phi_s = 50°$ at position RX5, we can see the 2D and 3D embedding results in Fig. 6. Indeed, the MPCs within the main beam direction are significantly impacted, showing the spatial filtering nature of the T-RIS.
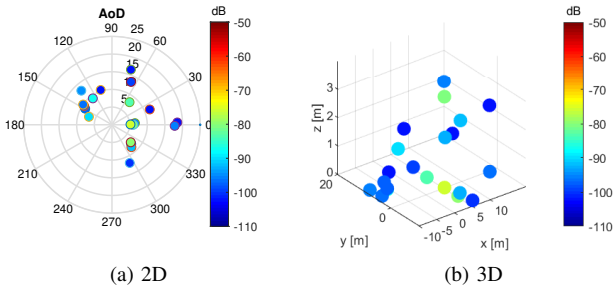

(a) 2D pattern embedding   (b) 3D pattern embedding

Fig. 5. PADP with T-RIS embedding for $\phi_s = 0°$.

(a) 2D pattern embedding   (b) 3D pattern embedding
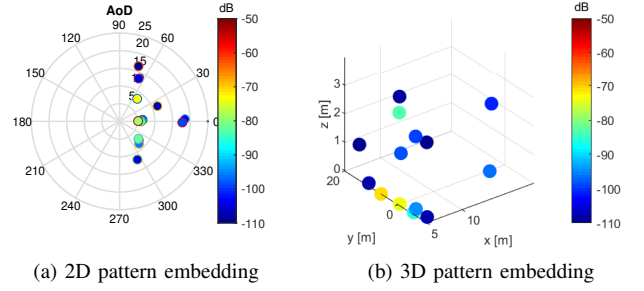
Fig. 6. PADP with T-RIS embedding for $\phi_s = 50°$.

In Fig. 7 and Fig. 8, we can see that the 3D embedding channels have higher channel gains and smaller DS than the T-RIS measured channels. Indeed the shape of the T-RIS measured and 3D embedding channels gains and DS follow a similar trend. The very smaller DS values for the 3D embedding channels are due to the consideration of only specular MPCs in the 3D embedding while the T-RIS measured channels include the DMCs.
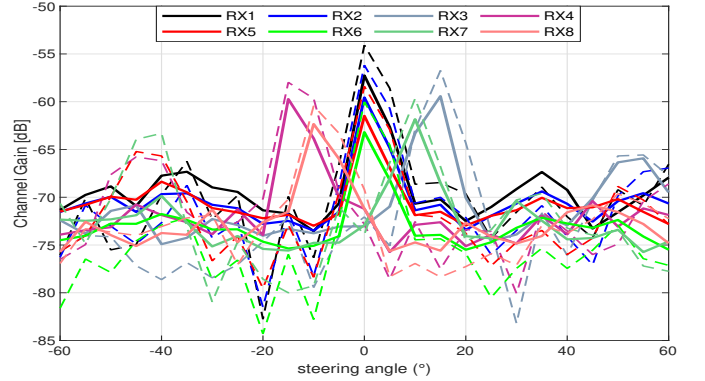

Fig. 7. Channel gain as a function of steering angle: measured (solid) vs 3D T-RIS embedding (dotted line).

(a) 2D   (b) 3D

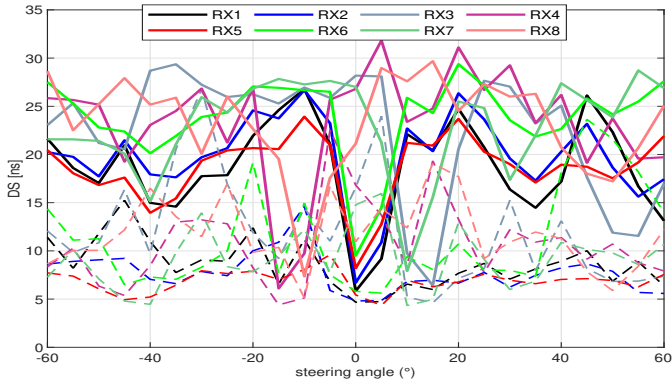Fig. 4. Omnidirectional PADP extracted from VCA measurements.

Fig. 8. Delay spread as a function of steering angle: measured (solid) vs 3D T-RIS embedding (dotted line)

With respect to the PDPs, Fig. 9 shows a comparison of the actual T-RIS measured channel PDP (in blue color) with the PDPs of synthesized channels (in red, green and black colors). The synthesized channels involve the plugging in or embedding of the measured 2D and simulated 3D T-RIS radiation patterns to the UWB SAGE extracted MPCs from the VCA measurement setup. From the aforementioned figures, we can observe that the 3D synthesized channel closely resembles the actual measured channel as it corrects the overestimation of secondary MPCs powers encountered in the 2D synthesized channels. It is worth mentioning that there is a 3 dBi peak gain difference between the 2D T-RIS measured gain pattern and the 3D T-RIS simulated gain patterns, with the latter being higher. As expected embedding in the 3D dimension improves the quality of the model especially for secondary MPCs that could come at elevation angles far from the azimuth plane.

However the process here involves only the MPCS that are extracted from UWB-SAGE, while it is well known that dense multipath components (DMCs) yeild an important energy contribution. Hence here we artificially add the DMCs extracted from VCA measurements to add them to the 3D synthesized channel. The PDP in black corresponds to the result of adding DMCs from the high resolution algorithm estimation to the 3D synthesized channel.
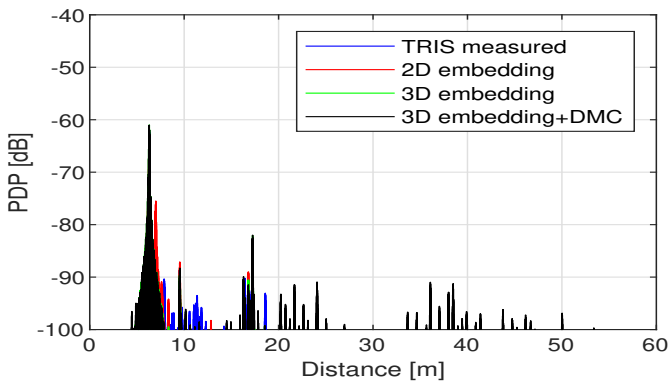

Fig. 9. Example of PDP comparison: actual measured PDP vs synthesized PDPs.

B. Large Scale Parameters

We employed the conventional power law model (4) to model the distance dependent channel gain:

$$G_{dB}(d) = G_0 - n \cdot 10 \cdot \log_{10}\left(\frac{d}{d_0}\right) + X_\sigma \qquad (4)$$

where G_0 is the intercept in dB at the reference distance d_0 set to 1 m. The path loss exponent n indicates the decrease in channel gain as a function of the distance d between the transmitter and receiver. Both G_0 and n are obtained from the intercept and slope of the best-fit to (4) according to the minimum mean square error. X_σ is the variation due to long-term fading effects and is characterized through a normal distribution with zero mean and a standard deviation σ in dB. Fig. 10 shows the channel gain comparison of the VCA measured channel, T-RIS measured channel and the synthesized channels in the maximum direction.

We can see that the VCA measured channel comprises the least channel gain and this is due to the presence of high gain T-RIS in the other cases. We can also see that the synthesized channel (considering the measured 2D T-RIS gain patterns), in red color, is lower compared to the actual measured T-RIS channel, in blue color, because the channel gain in the actual measured T-RIS channel includes the diffuse components which are not present in the synthesized channel. The synthesized channel considering measured 2D T-RIS gain pattern is also lower than the simulated 3D channel because of the 3dBi gain difference between the measured and the simulated T-RIS gains. The path loss model parameters are given in Tab. I. We observe that adding back the DMCs to the 3D embedding channel results in an improvement of the 3D model. The root mean square delay spread (DS), is the

TABLE I
PATH LOSS MODEL PARAMETERS.

Scenario	$G_0[dB]$	n	$\sigma[dB]$
VCA meas	-61.2	1.63	0.54
TRIS meas	-47.1	1.44	0.56
2D embedding	-49.9	1.54	1.1
3D embedding	-45.1	1.9	0.5
3D embedding +DMC	-46.7	1.4	0.8

TABLE II
DELAY SPREAD MODEL PARAMETERS.

Scenario	$a[ns/m]$	$b[ns]$	$\sigma_\tau[ns]$
VCA meas	0.33	9.6	1.54
TRIS meas	0.64	5.03	0.5
2D embedding	0.06	5.5	0.6
3D embedding	0.19	4	0.47
3D embedding + DMC	0.32	14.8	1.26

square root of the second central moment of the the power delay profile (PDP). For a multipath channel, the DS is a measure of duration of time over which most of the symbol

energy from the transmitter arrives to the receiver. The root mean square delay spread is calculated using the mean delay (the first moment of the PDP). To model the delay spread, we followed $\tau_{rms}[ns] = a \cdot d + b + X_\tau$ where a represents the delay spread, b is the intercept and X_τ denote a zero mean Gaussian random variable with standard deviation σ_τ. The delay spreads appear to increase with increasing transmitter-receiver separation distance. The delay spreads after adding back the DMCs are indeed higher as shown in the figure. In overall, the T-RIS cases (excluding the 3D embedding + DMC case) are characterized by lesser delay spreads than the VCA case and this is due to the high T-RIS gain and directivity. With regards to the angular spreads, not reported here for sake of briefness, we observed that the VCA channel is more spread in the azimuth plane (reaching values of over $50°$) and less spread in the elevation plane (values around $5°$) whereas the T-RIS synthesized cases are characterized by small angular spreads in both planes (less than $10°$).
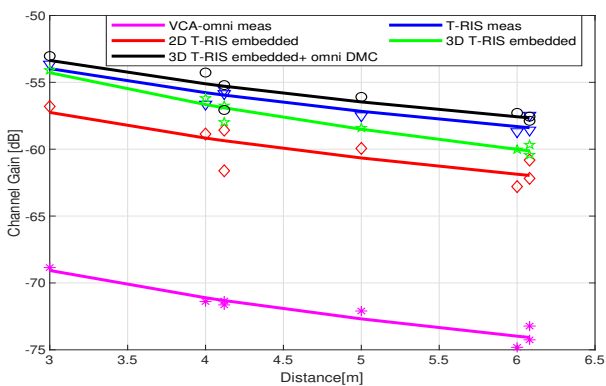

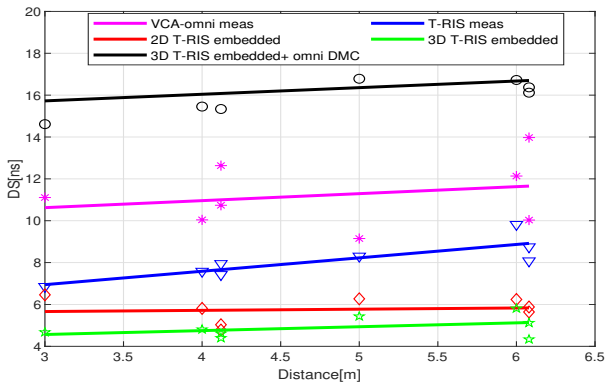Fig. 10. Channel gain comparison: measurements vs models.

Fig. 11. Delay Spreads comparison: measurements vs models.

V. Conclusions

In this paper we evaluated how the structure of the channel is geometrically modified when a transmitting reconfigurable surface is employed instead of omnidirectional monopole scanning spatial grids. Starting from the MPCs extracted from the Virtual Cubic Array measurement setup, we embedded

surface effect by knowing its radiation pattern for a given phase distribution and aimed steering angle. In our scenarios, the synthesized channel considering only the azimuth plane embedding (2D embedding) results in an overestimation of the powers of the secondary MPCs whose AoDs are within the half power beamwidth of the T-RIS. Performing 3D embedding, the synthesized channel highly resembles the actual T-RIS measured channel, since elevation information can effect multipath components amplitude. The large scale parameters showed that the high gain and directivity of the T-RIS results in reduced path losses, delay and angular spreads. However considering only specular components seems not enough to fully reproduce the measured results. As a first attempt we include dense multipath components (DMCs) to the 3D embedding channel improving path loss model, but delay spread is slightly overestimated. To further improve the quality of fitness, a full angular distribution of DMCs will also be considered.

References

[1] J. Huang, C.-X. Wang, R. Feng, J. Sun, W. Zhang, and Y. Yang, "Multi-frequency mmWave massive MIMO channel measurements and characterization for 5G wireless communication systems," *IEEE Journal on Selected Areas in Communications*, vol. 35, no. 7, pp. 1591–1605, 2017.

[2] A. L. Swindlehurst, E. Ayanoglu, P. Heydari, and F. Capolino, "Millimeter-wave massive MIMO: the next wireless revolution?" *IEEE Communications Magazine*, vol. 52, no. 9, pp. 56–62, 2014.

[3] A. De Domenico, R. Gerzaguet, N. Cassiau, A. Clemente, R. D'Errico, C. Dehos, J. L. Gonzalez, D. Ktenas, L. Manat, V. Savin, and A. Siligaris, "Making 5G Millimeter-Wave Communications a Reality [Industry Perspectives]," *IEEE Wireless Communications*, vol. 24, no. 4, pp. 4–9, 2017.

[4] E. G. Larsson, O. Edfors, F. Tufvesson, and T. L. Marzetta, "Massive mimo for next generation wireless systems," *IEEE communications magazine*, vol. 52, no. 2, pp. 186–195, 2014.

[5] P. Zhang, J. Chen, X. Yang, N. Ma, and Z. Zhang, "Recent research on massive MIMO propagation channels: A survey," *IEEE Communications Magazine*, vol. 56, no. 12, pp. 22–29, 2018.

[6] E. Basar, M. Di Renzo, J. De Rosny, M. Debbah, M. Alouini, and R. Zhang, "Wireless Communications Through Reconfigurable Intelligent Surfaces," *IEEE Access*, vol. 7, pp. 116 753–116 773, 2019.

[7] E. C. S. et al., "Wireless Environment as a Service Enabled by Reconfigurable Intelligent Surfaces: The RISE-6G Perspective," in *2021 Joint European Conference on Networks and Communications 6G Summit (EuCNC/6G Summit)*, 2021, pp. 562–567.

[8] A. Guerra, F. Guidi, D. Dardari, A. Clemente, and R. D'Errico, "A Millimeter-Wave Indoor Backscattering Channel Model for Environment Mapping," *IEEE Transactions on Antennas and Propagation*, vol. 65, no. 9, pp. 4935–4940, 2017.

[9] A. Mudonhi, M. Lotti, A. Clemente, R. D'Errico, and C. Oestges, "RIS-enabled mmWave Channel Sounding Based on Electronically Reconfigurable Transmitarrays," in *2021 15th European Conference on Antennas and Propagation (EuCAP)*, 2021, pp. 1–5.

[10] L. Di Palma, A. Clemente, L. Dussopt, R. Sauleau, P. Potier, and P. Pouliguen, "Circularly-polarized reconfigurable transmitarray in Ka-band with beam scanning and polarization switching capabilities," *IEEE Transactions on Antennas and Propagation*, vol. 65, no. 2, pp. 529–540, 2016.

[11] K. Haneda and J.-I. Takada, "An application of SAGE algorithm for UWB propagation channel estimation," in *IEEE Conference on Ultra Wideband Systems and Technologies, 2003*. IEEE, 2003, pp. 483–487.